$BiVO_4/Fe_3O_4$@polydopamine Superparticles for Tumor Multimodal Imaging and Synergistic Therapy

Ze Wang
Jilin University
Guan Wang
Jilin University Sino Japanese Hospital: China-Japan Union Hospital of Jilin University
Tingting Kang
Jilin University
Shuwei Liu
Jilin University
Lu Wang
Jilin University Stomatology Hospital
Haoyang Zou
Changchun Institute of Applied Chemistry Chinese Academy of Sciences: Chang Chun Institute of Applied Chemistry Chinese Academy of Sciences
Yu Chong
Soochow University
Yi Liu (yiliuchem@jlu.edu.cn)
State Key Laboratory of Supramolecular Structure and Materials, Jilin University, Changchun 130012, P. R. China https://orcid.org/0000-0003-0548-6073

Research

Keywords: Fe3O4 nanoparticles, BiVO4 nanoparticles, Superparticles, multimodal imaging, Synergy therapy

Posted Date: October 20th, 2020

DOI: https://doi.org/10.21203/rs.3.rs-92747/v1

Version of Record: A version of this preprint was published at Journal of Nanobiotechnology on March 29th, 2021. See the published version at https://doi.org/10.1186/s12951-021-00802-x.

Abstract

Background: Despite tremendous progress has been achieved in tumor theranostic over the past decade, accurate identification and complete eradication of tumor cells remain a great challenge owing to the limitation of single imaging modality and therapeutic strategy.

Results: Herein, we successfully design and construct $BiVO_4/Fe_3O_4$@polydopamine (PDA) superparticles (SPs) for computed tomography (CT)/photoacoustic (PA)/magnetic resonance (MR) multimodal imaging and radiotherapy (RT)/photothermal therapy (PTT) synergistic therapy toward oral epithelial carcinoma. On the one hand, $BiVO_4$ NPs endow $BiVO_4/Fe_3O_4$@PDA SPs with impressive X-ray absorption capability due to the high X-ray attenuation coefficient of Bi, which is beneficial for their utilization as radiosensitizers for CT imaging and RT. On the other hand, Fe_3O_4 NPs impart $BiVO_4/Fe_3O_4$@PDA SPs with the superparamagnetic property as a T_2-weighted contrast agent for MR imaging. Importantly, the aggregation of Fe_3O_4 NPs in SPs and the presence of PDA shell greatly improve the photothermal conversion capability of SPs, making $BiVO_4/Fe_3O_4$@PDA SPs as an ideal photothermal transducer for PA imaging and PTT. By integrating advantages of various imaging modalities (CT/PA/MR) and therapeutic strategies (RT/PTT), our $BiVO_4/Fe_3O_4$@PDA SPs exhibit the sensitive multimodal imaging feature and superior synergistic therapeutic efficacy on tumors.

Conclusion: Since there are many kinds of building blocks with unique properties appropriating for self-assembly, our work may largely enrich the library of nanomateirals for tumor diagnosis and treatment.

Background

Radiotherapy (RT) is one of the most widely used clinical strategies for cancer treatment.[1–4] More than 50% of cancer patients suffering from solid tumors are under treatment of RT.[5] Benefiting from the high intensity ionizing radiations (such as electrons, protons, and photons), RT can directly introduce deoxyribonucleic acid (DNA) double-strand breaks or yield a large number of cytotoxic reactive oxygen species (ROS) to trigger the apoptosis or necrosis of irradiated cancer cells.[6–9] However, the therapeutic efficacy of conventional RT is still limited by the insufficient radiation energy deposition on tumor tissues, as well as the serious toxic effects on normal surrounding healthy tissues.[10,11] Along with the development of nanotechnology and materials science, nanomaterials containing high-Z elements are exploited as radiosensitizers due to their high radiation energy deposition, thereby amplify the radiation-induced damage on tumor tissues, accompanied by the alleviation of the relevant side effects.[12–15] On the other hand, deriving from the abnormal blood vasculature, hypoxia is considered as the hostile feature of the tumor microenvironment (TME) to cause irreversible tumor metastasis and RT resistance.[16–18] As a novel therapeutic approach, photothermal therapy (PTT) is an efficient way to overcome this problem.[19–21] Under NIR light irradiation, photothermal agents not only generate regional hyperthermia to ablate cancer cells, but also promote the blood flow and oxygen pressure levels in tumor tissues, resulting in enhancing the tumor cell sensitivity to RT. Therefore, it is reasonable to believe that a

superior synergistic therapeutic efficacy from RT and PTT will be achieved by taking advantages of radiosensitizers and photothermal agents simultaneously.

It is well known that imaging techniques play the pivotal role in clinical diagnosis and efficacy evaluation.[22] Although various imaging techniques have been rapidly developed for many years, information collected by a single imaging modality is usually limited and insufficient due to the intrinsic restrictions of each modality.[23] For example, computed tomography (CT) imaging is good at constructing 3D visualization with anatomical details, but suffering from the low resolution.[24] Magnetic resonance (MR) imaging can scan objects with high resolution, but at the expense of the time-consuming data acquisition process.[25] Photoacoustic (PA) imaging is capable of providing the fast real-time monitor and unveils information with high signal-to-noise ratio, but only appropriate to soft tissues.[26] Hence, integrating different imaging modalities into a single nanostructure may hold great potentials to achieve complementary information for tumor diagnosis precisely, accurately and efficiently. Because of the high X-ray absorption coefficient (5.74 cm^2g^{-1} at 100 keV) and low cytotoxicity, bismuth (Bi)-based nanomaterials can be seen as an ideal radiosensitizer for CT imaging and RT.[27] In addition, due to the excellent superparamagnetic, Fe_3O_4 NPs have been approved by FDA for T_2-weighted MR imaging.[28] Most recently, it is reported that Fe_3O_4 NP aggregates exhibit an enhanced photothermal conversion capability comparing to their individual NPs owning to the collective effect.[29] The as-prepared Fe_3O_4 NP aggregates are also verified to have the potential to be used as the photothermal agents for PA imaging and PTT. Thus, constructing nanostructures containing Bi-based nanomaterials and Fe_3O_4 NPs is of great significance in realizing the multimodal imaging and synergistic therapy.

Self-assembly, which mainly depend on the supramolecular interactions (including van der Waals (vdW) interaction, electrostatic interaction, dipole interaction, hydrogen bonding, hydrophobic interaction and π-π stacking interaction) between building blocks, has been widely used to construct assemblies with different morphologies and formations.[30] During self-assembly, the intrinsic physical and chemical properties of the building blocks are usually passed to the resulting assemblies entirely, which offer us a simple and flexible method to construct nanostructures with desired compositions and functions.[31] Herein, we successfully design and prepare $BiVO_4/Fe_3O_4$@polydopamine (PDA) superparticles (SPs) for CT/PA/MR multimodal imaging and RT/PTT synergistic therapy. $BiVO_4$ and Fe_3O_4 NPs with the average sizes of 7.12 and 5.49 nm are firstly prepared, followed by their subsequent self-assembly into $BiVO_4/Fe_3O_4$ SPs via the oil-in-water microemulsion route. After that, the as-prepared $BiVO_4/Fe_3O_4$ SPs are covered by PDA to further improve their photothermal conversion capability. At last, the imaging and therapy performances of $BiVO_4/Fe_3O_4$@PDA SPs are evaluated via in vitro and in vivo experiments. The results clearly manifest that our $BiVO_4/Fe_3O_4$@PDA SPs can be seen as the promising nanomedicine for tumor theranostic with ideal accuracy and therapeutic efficacy.

Results And Discussion

$BiVO_4/Fe_3O_4$@PDA SPs are constructed upon the self-assembly of $BiVO_4$ and Fe_3O_4 NPs following by coating with the PDA shell. Typically, $BiVO_4$ NPs are prepared through our previous two-phase method, and Fe_3O_4 NPs are prepared via the classical thermal decomposition method.[32,33] Transmission electron microscopy (TEM) images in Fig. 1a and 1b show that both of $BiVO_4$ and Fe_3O_4 NPs are monodispersed nanospheres with the average diameters around 7.12 and 5.49 nm, respectively. High-resolution TEM (HRTEM) images exhibit the lattice fringes with the interplanar spacings of 0.312 and 0.244 nm, corresponding to the (112) planes of monoclinic $BiVO_4$ and the (311) planes of cubic Fe_3O_4. X-ray diffraction (XRD) patterns of $BiVO_4$ and Fe_3O_4 NPs further identify the monoclinic crystal structure of $BiVO_4$ NPs and the cubic crystal structure of Fe_3O_4 NPs (Fig. S1).

Then, oil-in-water microemulsion method is employed to construct $BiVO_4/Fe_3O_4$ SPs using $BiVO_4$ and Fe_3O_4 NPs as the building blocks while sodium dodecyl sulfate (SDS) as the surfactants.[34] The as-prepared SDS-capped $BiVO_4/Fe_3O_4$ SPs are nanospheres with the average diameter of 81.20 nm (Fig. 1c). The element distributions of $BiVO_4/Fe_3O_4$ SPs are characterized by energy-dispersive X-ray spectroscopy (EDS) elemental mapping (Fig. S2). Bi, V and Fe are uniformly distributed throughout the entire SPs, further demonstrating the assembled configuration of the as-prepared $BiVO_4/Fe_3O_4$ SPs. Benefiting from the flexibility of the self-assembly technique, the size and composition of $BiVO_4/Fe_3O_4$ SPs is tunable deliberately. For example, by increasing the toluene-to-water ratio from 1:5 to 2:5, the size of $BiVO_4/Fe_3O_4$ SPs can be increased from 81.20 to 164.50 nm (Fig. S3). In the meantime, upon adjusting the feeding ratio between $BiVO_4$ and Fe_3O_4 NPs during self-assembly, the molar ratio of Bi/Fe in the as-prepared $BiVO_4/Fe_3O_4$ SPs is varied from 3.5:1 to 1.2:1. The corresponding products are designated as $BiVO_4/Fe_3O_4$-1, $BiVO_4/Fe_3O_4$-2 and $BiVO_4/Fe_3O_4$-3 SPs (Table S1).

At last, dopamine (DA) monomers are oxidized followed by spontaneous polymerization on the surface of $BiVO_4/Fe_3O_4$ SPs under the alkaline condition.[35] The thickness of the PDA shell is positively correlated with the amount of DA, which will be increased from 10.00 to 80.00 nm when the concentration of DA increase from 0.3 to 0.8 mg/mL (Fig. S4). Given that nanomaterials larger than 120.00 nm can hardly enter into cells upon cellular phagocytosis, $BiVO_4/Fe_3O_4$ SPs with the diameter around 80.00 nm is selected as the core and the PDA shell thickness is designed to be around 10.00 nm.

Since the aggregation of Fe_3O_4 NPs and the presence of the PDA shell can remarkably increase the molar extinction coefficient of monodispersed Fe_3O_4 NPs (Fig. S5), leading to the enhancement in their photothermal conversion capability, the photothermal conversion capability of $BiVO_4/Fe_3O_4$@PDA SPs suspension is evaluated under 808 nm irradiation. As shown in Fig. 2a, the photothermal conversion capability of $BiVO_4/Fe_3O_4$@PDA SPs is enhanced by elevating the proportion of Fe_3O_4 in SPs. At the same time, the temperature of $BiVO_4/Fe_3O_4$@PDA SPs aqueous solution rises rapidly by increasing the power density of the applied laser and the concentration of SPs (Fig. 2b and 2c). Under 1 W/cm^2 irradiation for 10 min, the aqueous solution containing 200 μg/mL of $BiVO_4/Fe_3O_4$@PDA SPs exhibits a

noticeable temperature increment of 25 °C. Based on the reported model, the photothermal conversion efficiency of as-prepared $BiVO_4/Fe_3O_4$@PDA SPs is estimated to be 33.42%, which is comparable to previous reports (Fig. S6).[29] To balance the properties deriving from $BiVO_4$ and Fe_3O_4, $BiVO_4/Fe_3O_4$@PDA SPs with the Bi/Fe element ratio of 1.8/1 are selected for the following in vitro and in vivo experiments.

Prior to assessing the imaging performance of $BiVO_4/Fe_3O_4$@PDA SPs, their cytotoxicity is evaluated via standard Cell Counting Kit 8 (CCK-8) assay. After incubation with $BiVO_4/Fe_3O_4$@PDA SPs at different concentrations for 24 h, the cell viability of oral epithelial carcinoma (KB) cells is higher than 80% even at a high concentration of 300 μg/mL, which strongly manifest the negligible cytotoxicity of $BiVO_4/Fe_3O_4$@PDA SPs (Fig. S7). The colloidal stability of $BiVO_4/Fe_3O_4$@PDA SPs is tested as well. After storage in water, saline, cell culture or serum-containing cell culture for 24 h, $BiVO_4/Fe_3O_4$@PDA SPs are well dispersed without any visible coagulation (Fig. S8). The low toxicity plus the high colloidal stability provide a powerful guarantee for the utilization of $BiVO_4/Fe_3O_4$@PDA SPs in tumor theranostic.

Subsequently, the in vitro imaging performances of $BiVO_4/Fe_3O_4$@PDA SPs are exhibited in Fig. 3a-c. Owning to the high X-ray attenuation coefficient of Bi, the CT signal intensities of $BiVO_4/Fe_3O_4$@PDA SPs increase linearly and sharply with their concentrations. The Hounsfield units (HU) value of $BiVO_4/Fe_3O_4$@PDA SPs is calculated to be 28.2136 $HU{\cdot}mL{\cdot}mg^{-1}$, which is comparable to the clinically used CT contrast agent iobitridol (25.6570 $HU{\cdot}mL{\cdot}mg^{-1}$) (Fig. 3a). Further increasing the proportion of $BiVO_4$ in SPs can improve the CT imaging performance of $BiVO_4/Fe_3O_4$@PDA SPs undoubtedly, but may lose their PA and MR imaging performances as the price. In addition, $BiVO_4/Fe_3O_4$@PDA SPs are also anticipated to be the MR imaging contrast agents owing to the superparamagnetic property of Fe_3O_4 NPs. Their MR imaging contrast is enhanced in a concentration-dependent manner, and the r_2 value is estimated to be 186 $mM^{-1}{\cdot}s^{-1}$, which is higher than current commercial MR contrasts, such as Resovist (143 $mM^{-1}{\cdot}s^{-1}$) and Feridex (93 $mM^{-1}{\cdot}s^{-1}$) (Fig. 3b). Furthermore, benefiting from the excellent photothermal conversion capability, there is a good linear relationship between the concentration of $BiVO_4/Fe_3O_4$@PDA SPs and their PA signal under NIR irradiation, suggesting their great potentials as the PA contrast agents (Fig. 3c). Then, in vivo multimode CT/MR/PA imaging properties of $BiVO_4/Fe_3O_4$@PDA SPs are explored on the subcutaneous tumor model. As shown in Fig. 3d, the tumor tissue will possess the enhanced CT imaging signal after the intratumoral injection of $BiVO_4/Fe_3O_4$@PDA SPs. In contrast, only normal bone structures can be observed without the injection of $BiVO_4/Fe_3O_4$@PDA SPs. Meanwhile, the mouse treated by $BiVO_4/Fe_3O_4$@PDA SPs displays a clear T_2-weighted MR imaging in the tumor region comparing to the region without the SP injection (Fig. 3e). As for PA imaging, the PA signal of tumor is notably enhanced after intratumoral injection of $BiVO_4/Fe_3O_4$@PDA SPs. As a comparison, only extremely weak PA signal arising from the tumor blood can be detected in the tumor site without the injection of $BiVO_4/Fe_3O_4$@PDA SPs (Fig. 3f). The results above suggest the great potentials of $BiVO_4/Fe_3O_4$@PDA SPs in multimodal imaging, which could combine advantages of each technique to provide complementary information for accurate diagnosis.

Thereafter, the in vitro synergistic therapeutic effect of $BiVO_4/Fe_3O_4$@PDA SPs are evaluated via clonogenic assay (Fig. 4a and 4b). KB cells are treated by X-rays with different radiation doses (2 to 8 Gy) or NIR laser (0.33 W cm^{-2}) in the absence or presence of SPs (100 μg/mL). The result manifests that NIR alone and X-ray alone treatments can decrease the colony formation of KB cells to 88.2% and 61.3%, whereas SPs + NIR and SPs + X-ray can inhibit cell survival to 10.1% and 12.0%. Surprisingly, only 2.1% cells survive after the treatment of SPs + X-ray + NIR. Moreover, compared to the colony forming efficiency under X-ray treatment alone, the same therapeutic effect can be achieved under lower X-ray dose in the X-ray + NIR group, which strongly certify the considerable synergistic therapeutic efficacy between RT and PTT (Fig. 4c).

Next, 2',7'-dichlorodihydrofluorescein diacetate (DCFH-DA) fluorescent probe is employed to detect intracellular oxidative stress level of KB cells after different treatments.[36] As shown in Fig. 4d, there is no detectable fluorescence in cells treated by PBS, SPs, NIR or SPs + NIR. In contrast, cells under X-ray, SPs + X-ray, SPs + NIR + X-ray treatments exhibit the bright fluorescence, and their fluorescence intensities are gradually enhanced. Since high radiation energy deposition and enhanced oxidative stress may facilitate the damage of DNA, γ-H2AX staining is performed to analyze the damage of DNA double-strand in cell nuclei quantitatively (Fig. 4e).[37] As similar as the ROS assay, no visible fluorescence is found in cells without the X-ray treatment. The apparent fluorescence can be seen in cells under the treatments of X-ray, SPs + X-ray and SPs + NIR + X-ray, and the SPs + NIR + X-ray treatment produce the highest fluorescence intensity. Both DCFH-DA and γ-H2AX assays demonstrate the synergistic therapeutic efficacy of RT and PTT.

Motivated by the effective in vitro therapeutic outcome, the subcutaneous tumor model is employed to investigate the antitumor efficacy of $BiVO_4/Fe_3O_4$@PDA SPs in vivo. The KB tumor-bearing BALB/c nude mice are randomly divided into 7 groups according to various treatments: (1) PBS, (2) SPs, (3) NIR, (4) X-rays, (5) SPs + NIR, (6) SPs + X-rays, (7) SPs + NIR + X-rays. Mice in group (3), (5) and (7) are irradiated by an 808 nm laser (0.33 W/cm^2) for 10 min after the injection of $BiVO_4/Fe_3O_4$@PDA SPs. Fig. S9 exhibits the IR thermographs of mice at different time intervals. The temperature of tumor tissue treated by SPs exhibits a rapid increase of 19 °C within 10 min, which is sufficient for tumor ablation. In contrast, there is no significant temperature elevation in the tumor without SPs injection. This dramatic difference lead to the remarkable localized overheat at the tumor site under NIR irradiation, causing severe tumor damage without influencing the adjacent normal tissues. Tumor volumes within 16 days in each group are recorded (Fig. 5a). The tumor volumes in group (1), (2) and (3) increase rapidly, suggesting the negligible effect of SPs alone and NIR alone treatments on the inhibition of tumor growth. Tumors in group (4) grow slowly comparing with those in group (1), revealing the irradiation of X-ray can only inhibit the tumor growth mildly. Despite SPs + X-ray and SPs + NIR treatments have the significantly inhibition on the growth of tumor at the initial stage of treatment, there are recurrences can be found after the treatment for about 10 days. Surprisingly, nearly complete tumor inhibition is realized in group (7) in the absence of recurrence. The weights and photographs of tumors exhibited in Fig. 5b and 5c further verifies that the synergistic therapeutic efficacy of RT and PTT are better than any single treatment. Because the weights

of mice in each group are steady without distinct fluctuation, the side-effects of all the treatments during the therapeutic process can be excluded (Fig. 5e). According to the hematoxylin and eosin (H&E) staining images of tumor tissues (Fig. 5g), the death and nucleus rupture and ablation of cancer cells can be observed in tumors under SPs + X-ray and SPs + NIR treatments, whereas the tumors in group (7) have the most serious cell damage. This result further demonstrates the combination of RT with PTT can greatly improve the therapeutic effect compared to any single treatment. Besides the overlap of RT and PTT, the excellent synergistic therapeutic efficacy of $BiVO_4/Fe_3O_4$@PDA SPs on tumor inhibition may come from the alleviation of hypoxia status in tumor tissues by boosting intratumoral blood circulation under NIR irradiation. Fig. S10 shows the in vivo PA images of tumors under various treatments: (1) PBS, (2) NIR, (3) SPs, (4) SPs + NIR, which imply that the photothermal conversion capability of $BiVO_4/Fe_3O_4$@PDA SPs can remarkably increase tumor oxygenation, making tumor cells more sensitive to RT.

At last, the biosafety profile of $BiVO_4/Fe_3O_4$@PDA SPs is evaluated by using BALB/c nude mice. H&E staining assays of major organs show that different treatments have no significant effects in the organ tissues of heart, liver, spleen, lung and kidney (Fig. S11). Serum biochemistry analysis exhibits the negligible side-effects on blood glucose and lipid, liver and renal function tests after the injection of SPs and combined treatments (Fig. S12). All these results mentioned above testify the excellent biocompatibility and powerful lethality of $BiVO_4/Fe_3O_4$@PDA SPs.

Conclusion

In summary, we demonstrate on the design and preparation of $BiVO_4/Fe_3O_4$@PDA SPs by using $BiVO_4$ and Fe_3O_4 NPs as the building blocks. $BiVO_4$ NPs endow $BiVO_4/Fe_3O_4$@PDA SPs with impressive X-ray absorption capability due to the high X-ray attenuation coefficient of Bi, which is benefit for their utilization as radiosensitizers for CT imaging and RT. On the other hand, the superparamagnetic of Fe_3O_4 NPs strongly guarantee the application of $BiVO_4/Fe_3O_4$@PDA SPs as T_2-weighted contrast agent for MR imaging. Furthermore, the aggregation of Fe_3O_4 NPs in SPs and the presence of PDA shell greatly improve the photothermal conversion capability of SPs, making $BiVO_4/Fe_3O_4$@PDA SPs as an ideal photothermal transducer for PA imaging and PTT. By integrating the advantages of various imaging modalities (CT/PA/MR) and therapeutic strategies (RT/PTT), our $BiVO_4/Fe_3O_4$@PDA SPs exhibit the sensitive multimodal imaging capability and superior synergistic therapeutic efficacy for tumors. Since there are many kinds of building blocks with unique properties appropriating for self-assembly, our work may largely enrich the library of nanomateirals for tumor theranostic.

Methods

Materials:

$Bi(NO_3)_3{\cdot}5H_2O$ (99.0%, Aladdin), NH_4VO_3 (99.9%, Aladdin), $Fe(acac)_3$ (99.9%, Simga-Aldrich), oleyamine (OLA, 70%, Simga-Aldrich), 1,2-hexadecanediol (90%, Aladdin), oleic acid (OA, 90%, Simga-Aldrich), SDS

(99%, Simga-Aldrich), 1-octadecene (ODE, 90%, Simga-Aldrich), tris(hydroxymethyl) aminomethans (Tris, > 99%, Aladdin), DA (99.0%). γ-H2AX (phospho S139) antibody [EP854(2)Y] (Alexa Fluor 568) (ab206901) was purchased from Abcam. Crystal violet staining solution, CCK-8, hoechst 33342 and ROS assay kit were purchased from Beyotime.

Preparation of $BiVO_4$ NPs:

1 mmol $Bi(NO_3)_2 \cdot 5H_2O$, 2 mL OLA, 2 mL OA and 10 mL ODE were added into a 100 mL three-necked flask. The temperature was raised to 175 °C in nitrogen atmosphere under vigorous stirring. When the solution was completely clear, the solution was dropped to 130 °C, followed by the addition of 10 mL water containing 2 mmol NH_4VO_3. The resulting solution was heated at 100 °C for 5 min and cooled down to room temperature naturally. After that, the solution was uniformly mixed with ethanol, and the bottom aqueous layer of the mixture was discarded. The upper organic layer was mixed with water and ethanol for twice, and the bottom aqueous layer of the mixture was discarded. The final product was washed by ethanol for another three times and dispersed in toluene.

Preparation of Fe_3O_4 NPs:

OA-capped Fe_3O_4 NPs were prepared by the thermal decomposition route. 2 mmol $Fe(acac)_3$, 2 mL OA, 2 mL OLA, 5 mmol 1,2-hexadecanediol and 20 mL benzyl ether were added into a 100 mL three-necked flask. The mixture was heated at 200 °C for 30 min under nitrogen atmosphere, followed by reflux at 265 °C for 30 min. After that, the solution was dropped to room temperature naturally, and the product was washed for three times by ethanol and finally dispersed in toluene.

Preparation of SDS-capped $BiVO_4/Fe_3O_4$ SPs:

2 mL toluene containing 50 mg $BiVO_4$ NPs and 20 mg Fe_3O_4 NPs was added into 5 mL aqueous solution containing 10 mg SDS. After ultrasonic stirring for 10 min, the resulting emulsions were heated at 60 °C for another 30 min to evaporate toluene. After that, solution was centrifuge at 3000 r/min for 5 min, and the SDS-capped $BiVO_4/Fe_3O_4$ SPs were obtained.

Preparation of $BiVO_4/Fe_3O_4$@PDA SPs:

DA monomer was added into 10 mL Tris-buffer solution (10 mM, pH 8.5) containing 5 mg SDS-capped $BiVO_4/Fe_3O_4$ SPs. After stirring for 3 h, the reaction solution was centrifuged at 5000 r/min for 30 min. Then, $BiVO_4/Fe_3O_4$@PDA SPs were obtained.

Characterization:

TEM was taken on a Hitachi H-800 electron microscope (200 kV) coupled with a CCD camera. UV-vis absorption spectra were obtained using a Lambda 800 UV-vis spectrophotometer. HRTEM and EDS were performed on a JEM-2100F electron microscope at an acceleration voltage of 200 kV with an EDS detector. XRD was implemented on an Empyrean X-ray diffractometer with Cu K radiation (λ = 1.5418 Å).

Declarations

Ethics approval and consent to participate

Not applicable

Consent for publication

Not applicable

Availability of data and materials

All sequence data generated and analysed during the current study are available in the NCBI database under the project accession number PRJNA597946, (https://www.ncbi.nlm.nih.gov/sra/PRJNA597946).

Competing interests

The authors declare that they have no competing interests.

Funding

This work was supported by NSFC (No. 21875086, 21906110), JLU Science and Technology Innovative Research Team (2017TD-06), Y.C. appreciates the support from the Natural Science Foundation of Jiangsu Province (BK20170353).

Authors' contributions

ZW designed and carried out experiments and wrote the manuscript. TTK synthesized the $BiVO_4/Fe_3O_4$@Polydopamine Superparticles with supervision from HYZ and YL. GW obtained and analyzed data. SWL and LW completed most of the in vivo and in vitro experiments. HYZ, YC and YL proposed and supervised the project. All authors read and approved the final manuscript.

Author details

[a] *State Key Laboratory of Supramolecular Structure and Materials, Jilin University, Changchun 130012, P. R. China. *Address correspondence to yiliuchem@jlu.edu.cn*

[b] *Key Laboratory of Polymer Ecomaterials, Changchun Institute of Applied Chemistry, Chinese Academy of Sciences, Changchun 130012, P. R. China.*

[c] *State Key Laboratory of Radiation Medicine and Protection, School for Radiological and Interdisciplinary Sciences (RAD-X), Collaborative Innovation Center of Radiation Medicine of Jiangsu Higher Education Institutions, Soochow University, Suzhou, 215123, P. R. China.*

[d]*Department of Gastroenterology, China-Japan Union Hospital, Jilin University, Changchun 130033, P. R. China.*

[e]*Department of Oral Pathology, School and Hospital of Stomatology, Jilin University, Changchun 130021, P. R. China.*

[#]*These authors contributed equally to this work.*

Ze Wang: wze19@mails.jlu.edu.cn

Guan Wang: crownwang830@jlu.edu.cn

Tingting Kang: kangtt18@mails.jlu.edu.cn

Shuwei Liu: liushuwei1213@163.com

Lu Wang: wangl0120@163.com

Haoyang Zou: zzhhyy2004@126.com

Chong Yu: chongyu@suda.edu.cn

Yi Liu: yiliuchem@jlu.edu.cn

References

1. Bernier J, Hall EJ, Giaccia Radiation oncology: a century of achievements. Nat. Rev. Cancer. 2004;4:737-47.
2. Baumann M, Krause M, Hill R. Exploring the role of cancer stem cells in radioresistance. Nat. Rev. Cancer. 2008;8:545-54.
3. Zappa C, Mousa SA. Non-small cell lung cancer: current treatment and future advances. Transl. Lung Cancer R. 2016;5:288-300.
4. Weichselbaum RR, Liang H, Deng L, Fu Y. Radiotherapy and immunotherapy: a beneficial liaison? N Rev. Clin. Oncol. 2017;14:365-79.
5. Atun R, Jaffray DA, Barton MB, Bray F, Baumann M, Vikram B, Hanna TP, Knaul FM, Lievens Y, Lui TYM, Milosevic M, O'Sullivan B, Rodin DL, Rosenblatt E, Van DJ, Yap ML, Zubizarreta E, Gospodarowicz M. Expanding global access to radiotherapy. Lancet Oncol. 2015;16:1153-86.
6. Prasad P, Gordijo CR, Abbasi AZ, Maeda A, Ip A, Rauth AM, DaCosta RS, Wu XY. Multifunctional Albumin–MnO_2 Nanoparticles Modulate Solid Tumor Microenvironment by Attenuating Hypoxia, Acidosis, Vascular Endothelial Growth Factor and Enhance Radiation Response. ACS Nano. 2014;8:3202-12.

7. Antosh MP, Wijesinghe DD, Shrestha S, Lanou R, Huang YH, T Hasselbacher, Fox D, Neretti N, Sun S, Katenka N, Cooper LN, Andreev OA, Reshetnyak YK. Enhancement of radiation effect on cancer cells by gold-p Proc. Natl. Acad. Sci. 2015;112:5372-76.
8. Dufort S, Bianchi A, Henry M, Lux F, Duc GL, Josserand V, Louis C, Perriat P, Crémillieux Y, Tillement O, Coll JL. Nebulized Gadolinium-Based Nanoparticles: A Theranostic Approach for Lung Tumor Imaging and Radiosensitization. Small. 2015;11:215-21.
9. Wang H, Zeng ZC, Bui TA, DiBiase SJ, Qin W, Xia F, Powell SN, Iliakis Replication Protein A2 Phosphorylation after DNA Damage by the Coordinated Action of Ataxia Telangiectasia-Mutated and DNA-dependent Protein Kinase. Cancer Res. 2001;61:8554-63.
10. Liu Y, Ai K, Lu L. Nanoparticulate X-ray Computed Tomography Contrast Agents: From Design Validation to in Vivo Applications. Acc. Res. 2012;45:1817-27.
11. Lei P, Zhang P, Yuan Q, Wang Z, Dong L, Song S, Xu X, Liu X, Feng J, Zhang H. Yb^{3+}/Er^{3+}-Codoped Bi_2O_3 Nanospheres: Probe for Upconversion Luminescence Imaging and Binary Contrast Agent for Computed Tomography Imaging. ACS Appl. Mater. Interfaces. 2015;7:26346-54.
12. Dong X, Cheng R, Zhu S, Liu H, Zhou R, Zhang C, Chen K, Mei L, Wang C, Su C, Liu X, Gu Z, Zhao Y. A Heterojunction Structured WO_9-WSe_2 Nanoradiosensitizer Increases Local Tumor Ablation and Checkpoint Blockade Immunotherapy upon Low Radiation Dose. ACS Nano. 2020;14:5400-16.
13. Feng L, Dong Z, Liang C, Chen M, Tao D, Cheng L, Yang K, Liu Z. Iridium nanocrystals encapsulated liposomes as near-infrared light controllable nanozymes for enhanced cancer radiotherapy. Biomaterials. 2018;181:81-91.
14. Gong F, Chen J, Han X, Zhao J, Wang M, Feng L, Li Y, Liu Z, Cheng L. Core–shell TaO_x@MnO_2 nanoparticles as a nano-radiosensitizer for effective cancer radiotherapy. J Mater. Chem. B. 2018;6:2250-57.
15. Chen R, Liu H, Dong X, Zhu S, Zhou R, Wang C, Wang Y, Wang X, Su C, Gu Z. Semiconductor heterojunction-based radiocatalytic platforms for tumors treatment by enhancing radiation response and reducing radioresistance. Chem. Eng. J. 2020;394:124827.
16. Sahu A, Kwon I, Tae G. Improving cancer therapy through the nanomaterials-assisted alleviation of hypoxia. Biomaterials. 2020;228:119578.
17. Cheng Y, Kong X, Chang Y, Feng Y, Zheng R, Wu X, Xu K, Gao X, Zhang H. Spatiotemporally Synchronous Oxygen Self-Supply and Reactive Oxygen Species Production on Z-Scheme Heterostructures for Hypoxic Tumor Therapy. Adv. Mater. 2020;32:1908109.
18. Horsman MR, Overgaard J. Hyperthermia: a Potent Enhancer of Radiotherapy. Clin. Oncol. 2007;19:418-26.
19. Shen S, Chao Y, Dong Z, Wang G, Yi X, Song G, Yang K, Liu Z, Cheng L. ottom-Up Preparation of Uniform Ultrathin Rhenium Disulfide Nanosheets for Image-Guided Photothermal Radiotherapy. Adv. Funct. Mater. 2017;27:1700250.

20. Wang S, Li X, Chen Y, Cai X, Yao H, Gao W, Zheng Y, An X, Shi J, Chen H. A Facile One-Pot Synthesis of a Two-Dimensional MoS_2/Bi_2S_3 Composite Theranostic Nanosystem for Multi-Modality Tumor Imaging and Therapy. Adv. Mater. 2015;27:2775-2782.
21. Zhou J, Li M, Hou Y, Luo Z, Chen Q, Cao H, Huo R, Xue C, Sutrisno L, Hao L, Cao Y, Ran H, Lu L, Li K, Cai K. Engineering of a Nanosized Biocatalyst for Combined Tumor Starvation and Low-Temperature Photothermal Therapy. ACS Nano. 2018;12:2858-72.
22. Schwenzer NF, Springer F, Schraml C, Stefan N, Machann J, Schick F. Non-invasive assessment and quantification of liver steatosis by ultrasound, computed tomography and magnetic resonance. J. Hepatol. 2009;51:433-445.
23. Smith BR, Gambhir SS. Nanomaterials for In Vivo Imaging. Chem. Rev. 2017;117:901-986.
24. Yip SSF. Aerts HJWL. Applications and limitations of radiomics. Phys. Med. Biol. 2016;61:R150-66.
25. Iima M, Bihan DL. Clinical Intravoxel Incoherent Motion and Diffusion MR Imaging: Past, Present, and Future. Radiology. 2016;278:13-32.
26. Fu QR, Zhu R, Song JB, Yang HH, Chen XY. Photoacoustic Imaging: Contrast Agents and Their Biomedical Applications. Adv. Mater. 2019;31:1805875.
27. Hu X, Sun J, Li F, Li R, Wu J, He J, Wang N, Liu J, Wang S, Zhou F, Sun X, Kim D, Hyeon T, Ling D. Renal-Clearable Hollow Bismuth Subcarbonate Nanotubes for Tumor Targeted Computed Tomography Imaging and Chemoradiotherapy. Nano Lett. 2018;18:1196-204.
28. Wang Y, Guo Q, Su G, Cao J, Liu J, Zhang X. Hierarchically Structured Self-Healing Actuators with Superfast Light- and Magnetic-Response. Adv. Funct. Mater. 2019;29:1906198.
29. Chen O, Riedemann L, Etoc F, Herrmann H, Coppey M, Barch M, Farrar CT, Zhao J, Bruns OT, Wei H, Guo P, Cui J, Jensen R, Chen Y, Harris DK, Cordero JM, Wang Z, Jasanoff A, Fukumura D, Reimer R, Dahan M, Jain RK, Bawendi MG. Magneto-fluorescent core-shell supernanoparticles. Nat. Commun. 2014;5:5093.
30. He J, Huang X, Li YC, Liu Y, Babu T, Aronova MA, Wang S, Lu Z, Chen X, Nie Z. Self-Assembly of Amphiphilic Plasmonic Micelle-Like Nanoparticles in Selective Solvents. Am. Chem. Soc. 2013;135:7974-84.
31. Xia Y, Tang Z. Monodisperse inorganic supraparticles: formation mechanism, properties and applications. Chem. Commun. 2012;48:6320-36.
32. Dong C, Lu S, Yao S, Ge R, Wang Z, Wang Z, An P, Liu Y, Yang B, Zhang H. Colloidal Synthesis of Ultrathin Monoclinic $BiVO_4$ Nanosheets for Z-Scheme Overall Water Splitting under Visible Light. ACS Catal. 2018;8:8649-58.
33. Sun S, Zeng H. Size-Controlled Synthesis of Magnetite Nanoparticles. J. Am. Chem. Soc. 2002;124:8204-5.
34. Zhuang J, Wu H, Yang Y, Cao YC. Controlling Colloidal Superparticle Growth Through Solvophobic Interactions. Angew. Chem., Int. Ed. 2008;47:2208-12.

35. Tang L, Yang X, Yin Q, Cai K, Wang H, Chaudhury I, Yao C, Zhou Q, Kwon M, Hartman JA, Dobrucki IT, Dobrucki LW, Borst LB, Lezmi S, Helferich WG, Ferguson AL, Fan TM, Cheng J. Investigating the optimal size of anticancer nanomedicine. Proc. Natl. Acad. Sci. 2014;111:15344-49.
36. Zhu Y, Li W, Zhang Y, Li J, Liang L, Zhang X, Chen N, Sun Y, Chen W, Tai R, Fan C, Huang Q. Excessive Sodium Ions Delivered into Cells by Nanodiamonds: Implications for Tumor Therapy. Small. 2012;8:1771-9 .
37. Srinivas US, Tan BWQ, Vellayappan BA, Jeyasekharan AD. ROS and the DNA damage response in cancer. Redox Biol. 2019;25:101084.

Figures

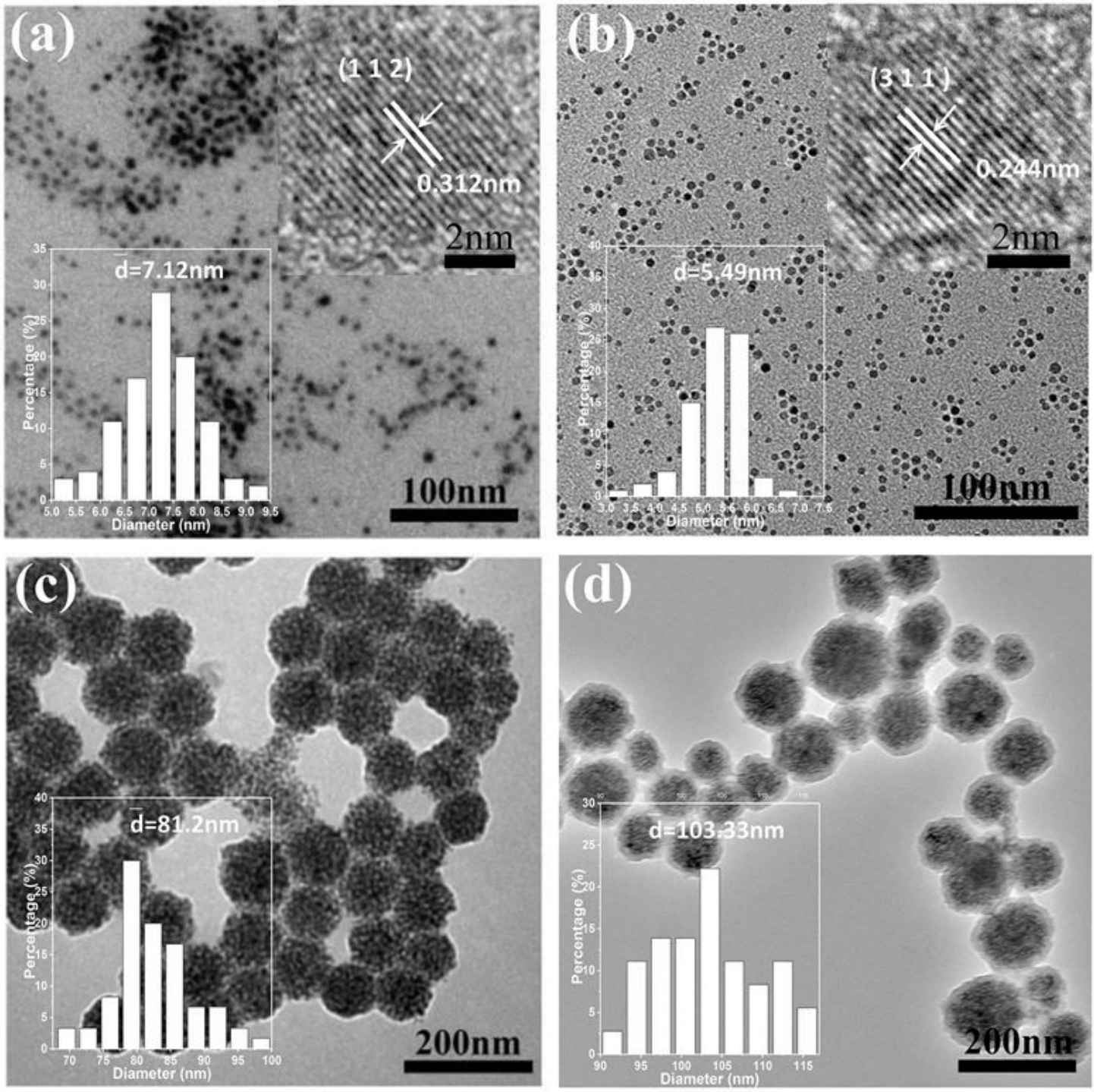

Figure 1

TEM images of (a) BiVO4 NPs, (b) Fe3O4 NPs, (c) BiVO4/Fe3O4 SPs and (d) BiVO4/Fe3O4@PDA SPs. Inset in (a) and (b): size distributions and HRTEM images of BiVO4 and Fe3O4 NPs. Inset in (c) and (d): size distributions of BiVO4/Fe3O4 SPs and BiVO4/Fe3O4@PDA SPs.

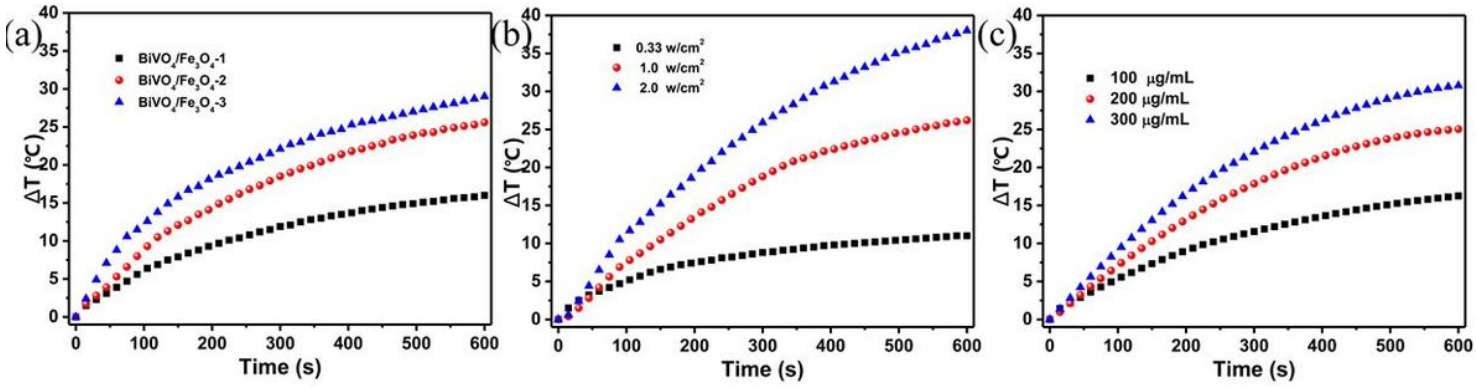

Figure 2

Temperature increments vs the proportions of Fe3O4 in BiVO4/Fe3O4@PDA SPs (200 μg/mL SPs; 1 W/cm2 irradiation) (a), the power densities of incident laser (200 μg/mL BiVO4/Fe3O4-2@PDA SPs) (b), the concentrations of SPs (BiVO4/Fe3O4-2@PDA SPs; 1 W/cm2 irradiation) (c).

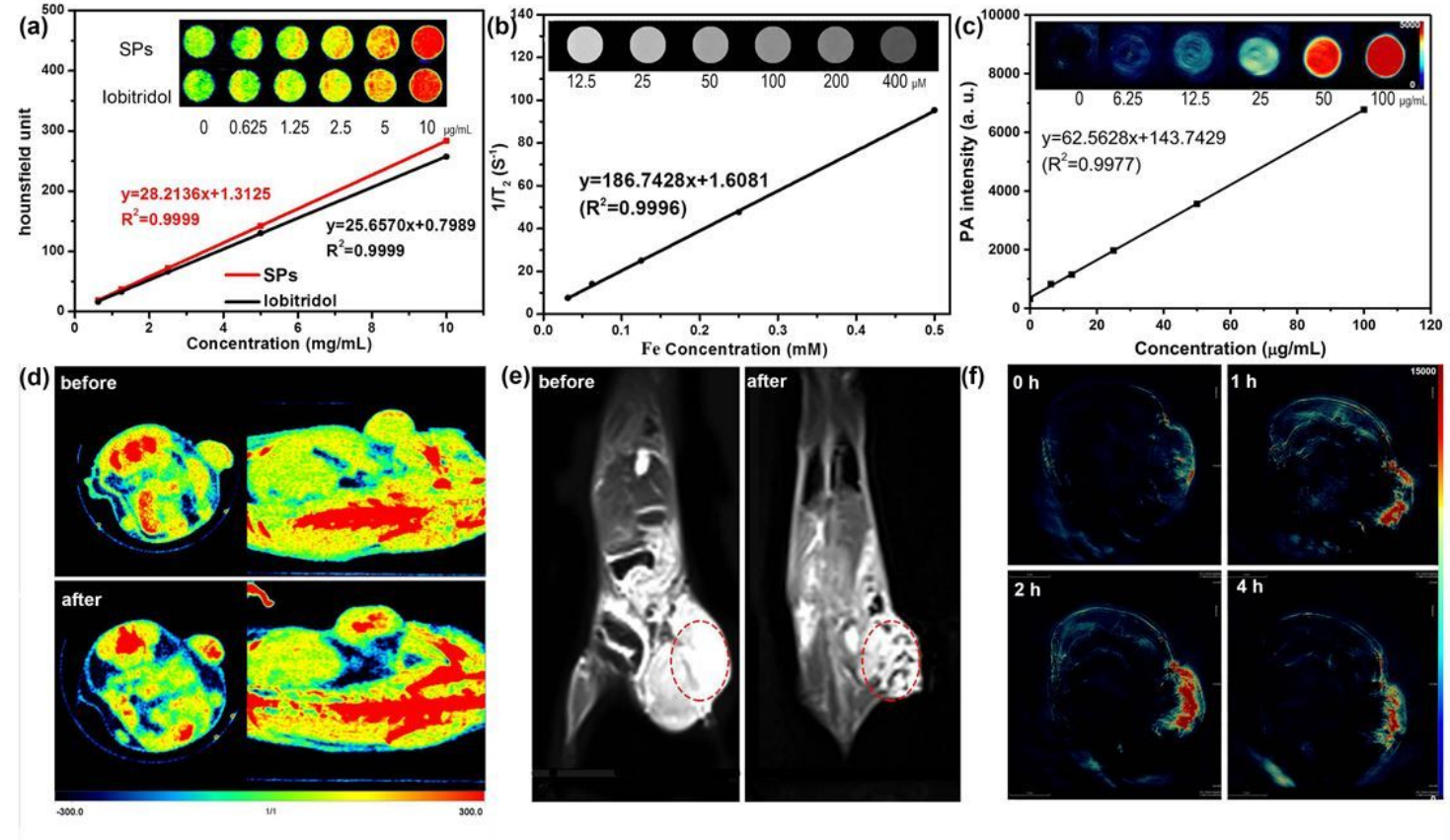

Figure 3

(a) In vitro CT images and HU values of BiVO4/Fe3O4@PDA SPs and iobitridol solution at different concentrations. (b) In vitro T2-weighted MR images and T2 relaxation rates of BiVO4/Fe3O4@PDA SPs at different concentrations. (c) In vitro PA images and PA values of BiVO4/Fe3O4@PDA SPs at different concentrations. In vivo CT (d), MR (e) and PA (f) images of mice bearing KB tumors obtained before and after intratumoral injection of BiVO4/Fe3O4@PDA SPs.

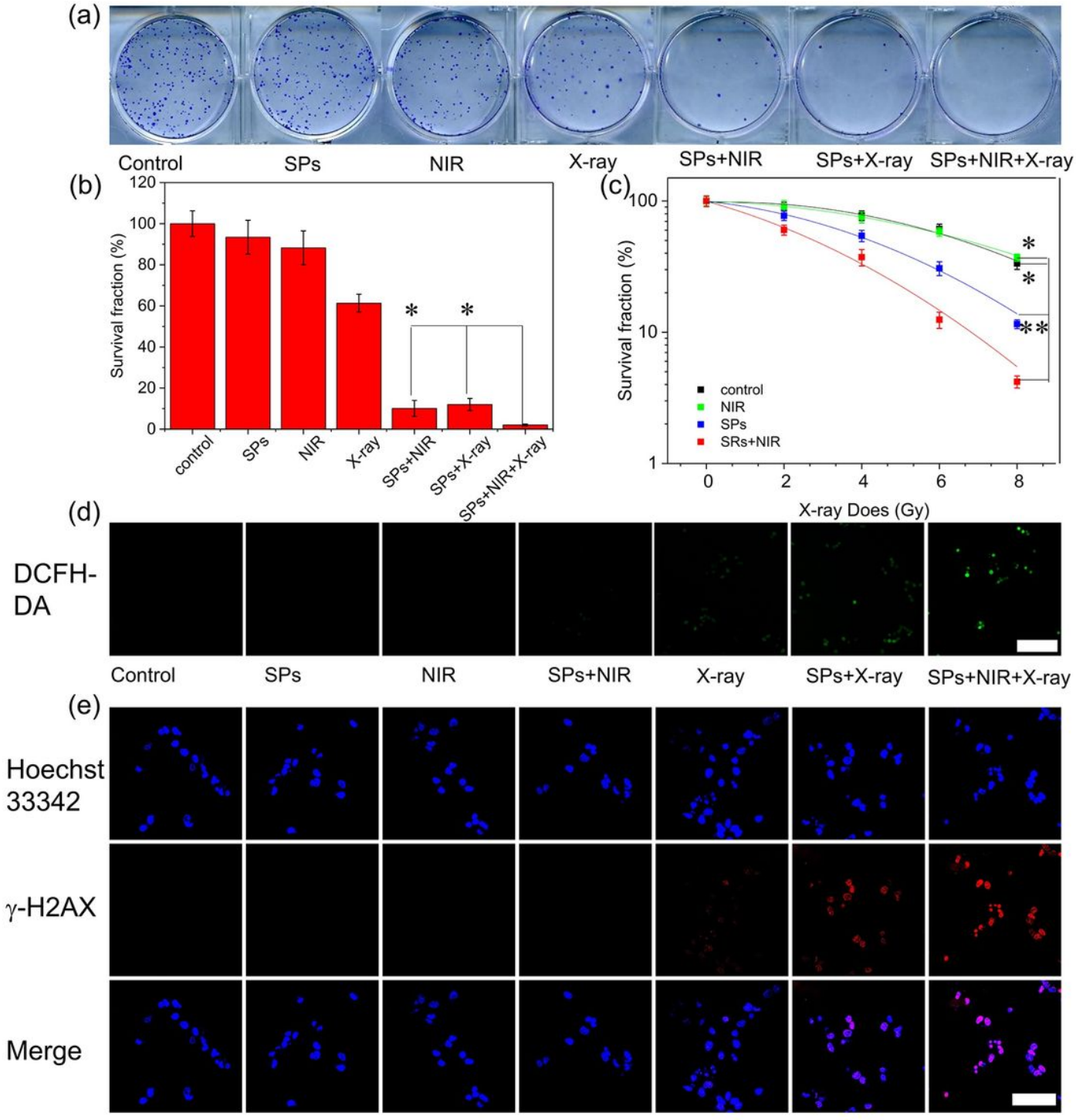

Figure 4

(a) Clonogenic assay of KB cells under different treatments (NIR: 0.33 W/cm2 and 10 min; X-ray: 6 Gy). (b) Survival fraction of KB cells under different treatments (NIR: 0.33 W/cm2 and 10 min; X-ray: 6 Gy). (c) Survival fraction of KB cells under different treatments and X-ray dose. (d) ROS production in KB cells under different treatments (scale bar is 200 μm). (e) γ-H2AX staining in KB cells under different treatments (scale bar is 40 μm). P-values were calculated by one-way ANOVA: *P < 0.05, **P < 0.01.

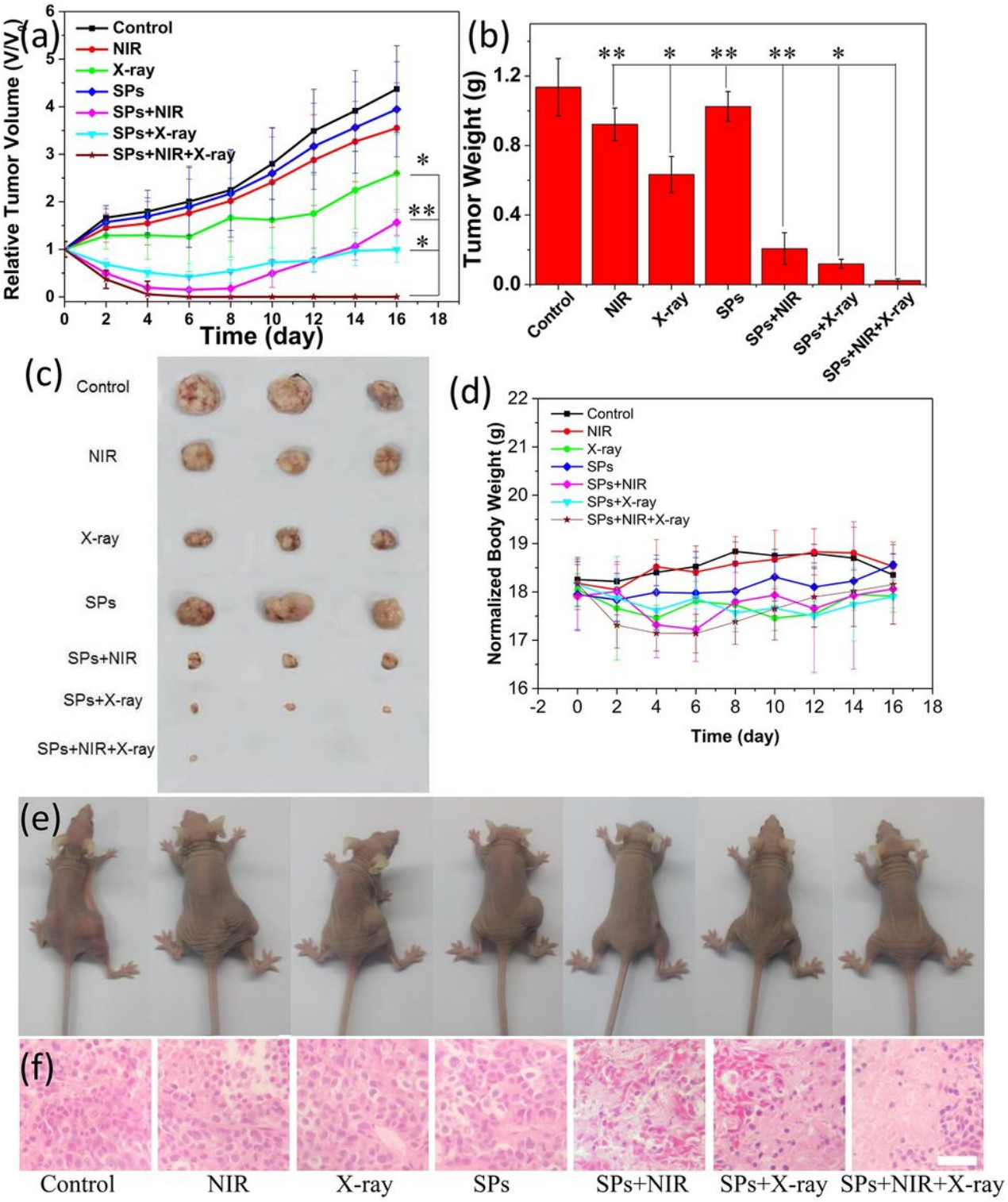

Figure 5

(a) Relative tumor volume curves of mice during 16 d. (b) Average tumor weights at the end of treatment. (c) Tumor photographs at the end of treatment. (d) Body weight curves of mice during 16 d. (e) Photographs of mice at the end of treatment. (f) H&E staining of tumor at the end of treatment (scale bar is 50 μm). P-values were calculated by one-way ANOVA: *P < 0.05, **P < 0.01.

Supplementary Files

This is a list of supplementary files associated with this preprint. Click to download.

- SupportingInformation.docx